Subcritical asymmetric Rayleigh breakup of a charged drop induced by finite amplitude perturbations in a quadrupole trap

Mohit Singh, Neha Gawande, Y. S. Mayya, and Rochish Thaokar [*]
Department of Chemical Engineering, Indian Institute of Technology Bombay, Mumbai 400076, India

The breakup pathway of Rayleigh fission of a charged drop is unequivocally demonstrated by continuous, high-speed imaging of a drop levitated in an AC quadrupole trap. The experimental observations consistently exhibited asymmetric, subcritical Rayleigh breakup with an upward (i.e., opposite to the direction of gravity) ejection of a jet from the levitated drop. These experiments supported by numerical calculations show that the gravity induced downward shift of the equilibrium position of the drop in the trap causes significant, large amplitude shape oscillations superimposed over the center-of-mass oscillations. The shape oscillations result in sufficient deformations to act as triggers for the onset of instability below the Rayleigh limit (a subcritical instability). The concurrently occurring, center-of-mass oscillations, which are out of phase with the applied voltage, are shown to lead to an asymmetric breakup such that the Rayleigh fission occurs upwards via the ejection of a jet at the pole of the deformed drop. As an important application, it follows by inference that the nanodrop generation in electrospray devices will occur, more as a rule rather than as an exception, via asymmetric, subcritical Rayleigh fission events of microdrops due to inherent directionality provided by the external electric fields.

I. INTRODUCTION

A charged drop of radius r_d undergoes Rayleigh instability when the total charge on the drop exceeds a critical value, $Q_R = 8\pi\sqrt{\epsilon_e \gamma r_d^3}$, where ϵ_e is the electrical permittivity of the medium and γ is the surface tension [1]. At this critical charge the repulsive Coulombic force just balances the restoring surface tension force of the droplet. The Rayleigh instability is believed to be responsible for the breakup of raindrops in thunderstorms [2], the formation of subnanometer droplets in electrosprays, and generation of ions in ion mass spectrometry [3]. Although the theoretical limit of the critical charge has been known for more than a hundred years [1], the breakup pathway was explicitly demonstrated only recently by Duft *et al.* (2003) [4] through systematic experiments on a levitated charged drop in a quadrupolar trap. Their experiments indicate that a critically charged drop sequentially deforms to an elongated prolate spheroid, eventually forming conical tips at its poles from which two jets are ejected in opposite directions. These jets carry 30–40% of original charge and negligible mass ($\sim$1%) [4,5]. The loss of charge reduces the electric stresses acting on the droplet and the deformed drop relaxes back to a spherical shape. The symmetrical jet ejection of a droplet tightly levitated in a quadrupole trap may not correspond to practical situations such as electrosprays, wherein unbalanced external forces such as gravity or an external electric field are most likely to introduce asymmetric breakup. The broken symmetry can have a tangible impact on the pathway of drop deformation as well as on the char-

acteristics of daughter droplets formation. A significant body of theoretical literature, both analytical [6–9] and numerical [10–14], indicates that instability of a charged droplet is subcritical with respect to "finite amplitude" prolate spheroidal perturbations. In this study, we provide experimental evidence for asymmetric, subcritical breakup through a combination of controlled observations and numerical simulations on levitated drops placed in external electric fields.

II. EXPERIMENTAL SETUP

A. Materials and method

The experiments were conducted by electrospraying (in dripping mode) a *positively* charged droplet of an ethylene glycol-ethanol mixture (50% v/v), into a quadrupole trap. NaCl is added to increase the electrical conductivity (σ) of the droplet, which is measured using a conductivity meter (Hanna instruments, HI 2316), and the viscosity (μ_d) of the droplets is measured using an Ostwald viscometer. The surface tension (γ) of the droplet is measured using a pendant drop (DIGIDROP, model DS) method, and the values obtained are reconfirmed with the spinning drop apparatus (dataphysics, SVT 20). The experiments are carried out at normal atmospheric conditions [1 atm pressure and 25 °C temperature as measured by using a VARTECH instrument (THM-B2)]. The temperature is maintained using a room air conditioner and temperature in the vicinity of the setup was measured and found to remain unchanged at 26 °C during the course of the experiment. The relative humidity is measured using a VARTECH instrument (THM-B2) and found to be around 20%.
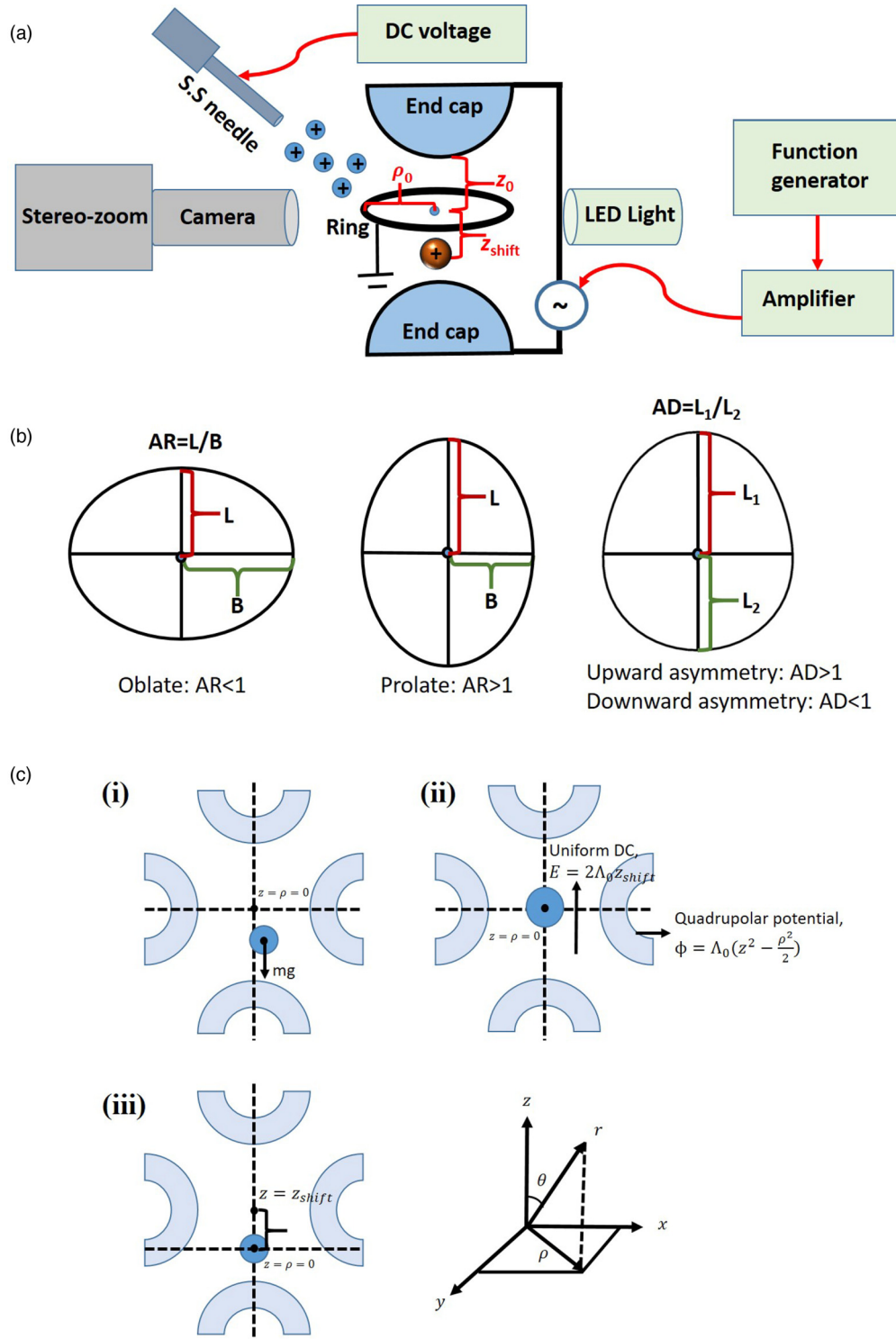
----

[*]rochish@che.iitb.ac.in

FIG. 1. (a) Schematic of the experimental setup used for studying the generation, levitation, and imaging of a charged drop in an electrodynamic balance. (b) Schematic of various lengths used for calculation of AR and AD. (c) Schematic depicting the typical analysis setup used for (i) center of mass motion [Eq. (8)], (ii) surface oscillations [Eqs. (9)–(11)] and (iii) breakup of droplet (BEM simulations).

The quadrupole trap used in the present experiments consists of two end-cap electrodes, which are shorted and separated by 20 mm ($= 2z_0$), and a ring electrode of the same diameter ($2\rho_0$) (such that $\rho_0 = z_0$), as shown in Fig. 1(a).

A function generator (33220A Function/Arbitrary Waveform Generator, 20 MHz) is connected to a high-voltage amplifier source (Trek, model 5/80, high-voltage power amplifier). This assembly is used to apply the potential of the desired wave

form between the electrodes. The applied peak to peak AC potential in our experiments is 11 kV with frequency varying from 0.1 to 0.5 kHz.

In a typical experiment, charged droplets are generated using electrospray realized by applying high DC voltage (6–7 kV) to a syringe tip. These charged droplets are then injected between the electrodes and are stabilized by the quadrupolar AC electric field between the end cap and the ring electrodes of the trap, resulting in their electrodynamic levitation. Single charged drop levitation is achieved by simultaneously levitating a few drops in the trap by a series of injection and stabilization episodes. The process is rendered quite systematic by adjusting the potential applied to the syringe tip or by adjusting the trapping potential and frequency. After suspending the desired number of drops within the trap, the potential applied to the syringe tip is switched off, eliminating any further injection of the droplet cloud. A single droplet is made to survive in the trap, by eliminating (destabilizing) all the other drops by appropriately adjusting the driving frequency of the trap. The levitated single droplet is observed using a high-speed CMOS camera (Phantom V 12, Vision Research, USA), which is connected with a stereo zoom microscope (SMZ1000, Nikon Instruments Inc.). The camera is kept inclined at 30°–40° with respect to the plane of the ring electrode. The error in the droplet diameter due to camera inclination is observed to be ~2%. Nikon halogen light (150 W) is used as a light source.

The shape deformations are characterized by two shape parameters; namely, aspect ratio (AR) and asymmetric deformation (AD), where AR indicates the symmetric deformation while AD is the measure of asymmetry in the shape of the drop. Thus, AR is defined as the ratio of the major axis (L) to the minor axis (B) such that when AR > 1 the shape is termed prolate and when AR < 1 the shape is called oblate, as shown in Fig. 1(b). The asymmetric deformation AD = L_1/L_2, where, L_1 and L_2 are the distances of north pole and south pole from the centroid respectively [Fig. 1(b)]. Note that the centroids are calculated using two-dimensioal images in IMAGEJ. We define the gravity acting from north to south and appropriately call the end caps the north and south end caps, and the poles of the droplet north and south poles. The charge on the droplet before and after the breakup is measured by the cutoff frequency method and also verified by the transient displacement method. The details of the methods can be found in our previous work [15]. With this experimental setup three types of analyses are carried out in this paper and the setups used for these analyses are depicted in Fig. 1(c).

B. Distribution of electric potential in quadrupole trap

The potential of an ideal quadrupole trap is given by $\phi = \Lambda(z^2 - \rho^2/2) = \Lambda r^2 P_2(\cos\theta)$, where $\Lambda = \Lambda_0\zeta(t)$, where $\zeta(t) = \cos(2\pi ft)$ is a time-periodic function of frequency f while (z, ρ) and (r, θ) stand for cylindrical and spherical polar coordinates respectively. Thus $r^2 = \rho^2 + z^2$ and $\rho^2 = x^2 + y^2$.

Here, $\Lambda_0 = \phi_0/(\rho_0^2 + 2z_0^2)$ (where ϕ_0 is the applied potential) is the intensity of an ideal quadrupole potential. Unlike the case of an ideal Paul trap, where $\rho_0 = \sqrt{2}z_0$, the present electrodynamic balance has $\rho_0 = z_0 = 10$ mm. Since our

electrodynamic balance is not an ideal Paul trap, the intensity of applied potential (Λ_0) is obtained by solving the electrostatic equation for the exact geometry of the setup in COMSOL MULTIPHYSICS software. The obtained data of the potential along ρ ($0 < \rho < 3$ mm) and z ($0 < z < 1$ mm) axes [$\phi(\rho, z)$] is then fitted into the equation of an ideal quadrupole trap by multilinear regression method using ORIGIN (version 9.1.0 Sr2, b271) software and the value of R^2 is found to be 0.99. Thus the potential distribution represented by

$$\phi = \Lambda_0\Big[z^2 - \frac{\rho^2}{2}\Big] \tag{1}$$

has the value of $\Lambda_0 \sim 1.76 \times 10^7$ V/m^2 and is used in the numerical calculations presented in the next sections. The electric field at the center of such a trap, $\rho = z = 0$, is 0. For an ideal Paul trap, the value of Λ_0 can be obtained from the definition, $\Lambda_0 = \frac{\phi_0}{r_0^2 + 2z_0^2}$. For $\phi_0 = 5500$ V, $r_0 = 10$ mm, and $z_0 = 10$ mm the value of $\Lambda_0 = 1.83 \times 10^7$ V/m^2. The difference between the values obtained from the fitting and from the definition is about 4%. The details of the fitting procedure are discussed in our earlier work [15].

III. BOUNDARY ELEMENT FORMALISM FOR DROPLET BREAKUP

To understand the mechanism of droplet breakup, numerical calculations are performed for a perfectly conducting liquid drop of radius r_d, suspended in a dielectric medium (air) in the presence of a quadrupole electric field. In this study, the Stokes equation for flow field and the Laplace equation for the electric potential (ϕ) are solved using the axisymmetric boundary element method (BEM). Here, all the quantities in the units of length are nondimensionalized by r_d, and the time, velocities, and stresses are scaled by $\mu_d r_d/\gamma$, γ/μ_d, and γ/r_d respectively, where γ is the interfacial tension. The charge and electric fields are scaled by $\sqrt{r_d^3\gamma\epsilon_a\epsilon_0}$ and $\sqrt{\gamma\epsilon_a\epsilon_0/r_d}$ respectively such that the nondimensional Rayleigh charge is $Q = 8\pi$. Thus the governing nondimensional electrohydrodynamic equations can be written as

$$\nabla^2\phi = 0, \tag{2}$$

$$\mathbf{\nabla} \cdot \mathbf{v}_{d,a} = 0, \tag{3}$$

$$-\mathbf{\nabla}p_{d,a} + \chi_{d,a}\nabla^2\mathbf{v}_{d,a} = 0, \tag{4}$$

where subscripts d and a represent drop (internal medium) and air (external medium) respectively. $p_{d,a}$ is the pressure, and χ denotes the viscosity parameter. Here, $\chi_a = 1$ for external medium and $\chi_d = \lambda = \mu_d/\mu_a$ inside the drop. As the droplet conductivity is high ($\sigma > 50$ μS/cm) in most of the experiments, the ratio of charge relaxation timescale ($\epsilon_d\epsilon_0/\sigma_d$) to the hydrodynamic timescale ($\mu_d r_d/\gamma$) is quite small ($\lesssim 10^{-3}$). Hence, charge relaxation may be considered instantaneous and accordingly the droplet is modeled as a perfect conductor.

In this framework, the governing equations are then transformed into integral equations and are solved using standard methods reported in our previous works [12,16,17]. The integral equation of the electric potential for a perfect conductor

drop is given by

$$\phi(\mathbf{r_s}) = \phi_0(\mathbf{r_s}) + \frac{1}{4\pi} \int \frac{E_{ne}(\mathbf{r})}{|\mathbf{r} - \mathbf{r_s}|} dS(\mathbf{r}), \qquad (5)$$

where E_{ne} is the normal component of the electric field ($\mathbf{n} \cdot \mathbf{E}$) with $\mathbf{n}$ as an outward normal, $\mathbf{r}$ and $\mathbf{r_s}$ are the position vectors on the surface of the drop, called the field and singular points respectively, and ϕ_0 is the applied electric potential which can be written as

$$\phi_0(\rho, z) = \sqrt{\mathrm{Ca}_\Lambda} \left[(z - z_{\mathrm{shift}})^2 - \frac{\rho^2}{2} \right]. \qquad (6)$$

$\mathrm{Ca}_\Lambda = (r_d^3 \epsilon_e / \gamma) \Lambda_0^2$ is the electric capillary number where Λ_0 is the strength of the applied quadrupole potential. Here z_{shift} accounts for the shifted position of the droplet from the center of the quadrupole trap. For convenience of calculations in these numerical simulations, the trap center is moved instead of the drop position, as reflected in the equation of the trap potential [Eq. (6)]. Thus the center of the drop coincides with the origin ($z = \rho = 0$), and z_{shift} is kept constant during the calculations. Since the breakup time is much smaller than the period of applied AC field (ω^{-1}), typical breakup times are of the order of few tens of microseconds while the frequencies applied are of the order of 100–300 Hz (timescales of 1–10 ms), the external potential (absorbed in $\sqrt{\mathrm{Ca}_\Lambda}$) is assumed to be DC such that the end caps are at positive potential for a positive value of $\sqrt{\mathrm{Ca}_\Lambda}$. Thus Eq. (6) represents a DC potential, with $\zeta(t) = 1$. Moreover, during this short time of breakup, the droplet is assumed to be quasistationary with respect to center of mass, and gravitational effects are ignored. The unknown potential $\phi(\mathbf{r_s})$ is constant on the surface of the drop, and is determined by the condition of conservation of charge given by $\int E_{ne}(\mathbf{r}) dS(\mathbf{r}) = Q$, where Q is the constant surface charge on the drop. The force density is then given by $\Delta \mathbf{f} = \mathbf{n} \nabla \cdot \mathbf{n} - [\tau_e]$, where $[\tau_e] = (1/2) E_{ne}^2$ is the normal electric stress acting on the drop surface. A small shape deformation is introduced initially via a function of the form $r_s(\theta) = r_d (1 + \sum_{l=1}^4 \alpha_l P_l(\cos\theta))$, where P_l is the lth Legendre mode and α_l is the corresponding coefficient. The force density is then used in the integral equation of interfacial velocity, which is given by

$$\mathbf{v}(\mathbf{r_s}) = -\frac{\lambda}{4\pi(1+\lambda)} \int \Delta \mathbf{f}(\mathbf{r}) \cdot G(\mathbf{r}, \mathbf{r_s}) dS(\mathbf{r})$$
$$+ \frac{(1-\lambda)}{4\pi(1+\lambda)} \int \mathbf{n}(\mathbf{r}) \cdot T(\mathbf{r}, \mathbf{r_s}) \cdot \mathbf{v}(\mathbf{r}) dS(\mathbf{r}), \qquad (7)$$

where $G(\mathbf{r}, \mathbf{r_s}) = \frac{1}{|\mathbf{x}|} + \frac{\mathbf{xx}}{|\mathbf{x}|^3}$ and $T(\mathbf{r}, \mathbf{r_s}) = -6\frac{\mathbf{xxx}}{|\mathbf{x}|^5}$ are the kernel functions with $\mathbf{x} = (\mathbf{r} - \mathbf{r_s})$ and are extensively discussed in the literature [18,19]. The shape of the drop is then evolved with time using an explicit Euler scheme. The details of the numerical scheme adopted in this study can be found in [17]. To summarize, the numerical calculations are aimed at explaining the asymmetric deformation and breakup without attempting to describe the center-of-mass (CM) or surface oscillations.
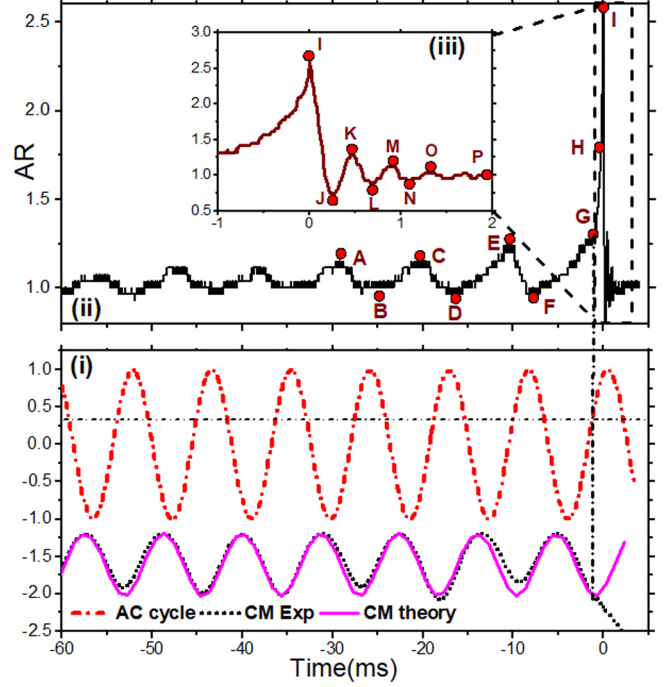

FIG. 2. The detailed mechanism of droplet center-of-mass motion, surface oscillation, breakup, and relaxation observed in a single high-speed video of a single drop, where inset figures represent (i) experimental and theoretical CM [obtained by solving Eq. (8)] oscillation dynamics in comparison with the normalized applied AC cycle, (ii) experimental observation of the drop deformation dynamics in terms of AR, and (iii) the enlarged region near the breakup and subsequent relaxation of the drop. The intersection of vertical and horizontal black dash-dotted lines indicates the point of instability with respect to the AC cycle. The red dots labeled A–P are used to indicate the various stages of the droplet evolution, and corresponding shapes are given in Fig. 3. Parameters: $\mu_d = 6.0$ mPa s, $r_d = 108$ μm, $\gamma = 30$ mN/m, $z_{\mathrm{shift}} = 500$ μm, $\mu_a = 0.0185$ mPa s, $f = 114$ Hz, $\rho_d = 960$ kg/m^3, and $\Lambda_0 = 1.76 \times 10^7$ V/m^2.

IV. RESULTS

In a typical experiment reported in this work, a charged droplet, under the influence of gravity, gets levitated at an off-centered position in the quadrupole electrodynamic (ED) balance, as shown in Fig. 1(a). Unlike the ion trap in vacuum [3], which operates at GHz frequency, the present setup operates at sub-kHz frequencies for levitating charged droplets at normal atmospheric pressure. It takes several minutes for the levitated droplets to evaporate to the point of attaining Rayleigh critical charge and undergo breakup. The events are recorded using a high-speed camera at speed in the range of $1 \times 10^5 - 2 \times 10^5$ frames per second (FPS) for about 2–4 seconds. The video is played back to analyze droplet center-of-mass (CM) oscillations [Fig. 2(i)], shape deformations, and the asymmetric breakup event [Fig. 2(ii)] and its relaxation back to original spherical shape after the breakup [Fig. 2(iii)]. The image sequence shown in Fig. 3 clearly indicates all these stages of breakup.

The droplet is seen to undergo simultaneous CM motion and shape deformations leading to an asymmetric breakup predominantly in the upward direction (that is, at the north
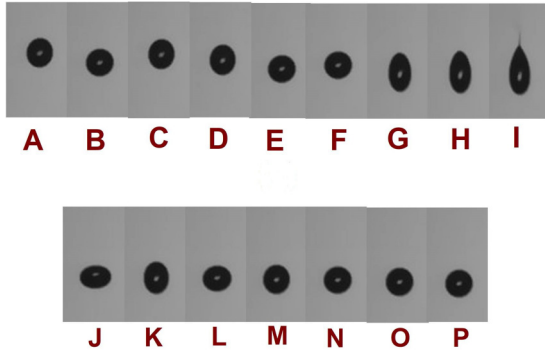
FIG. 3. Sequence of experimental images showing center-of-mass motion, deformation, breakup, and shape relaxation. The sequence of images A–F depicts CM and surface oscillations, images G and H show continuous deformation, image I indicates breakup, and images J–P correspond to relaxation of the drop shape after breakup. The timescales of the images are A: −29.1 ms; B: −24.9 ms; C: −20.2 ms; D: −16.4 ms; E: −10.2 ms; F: −7.8 ms; G: −0.95 ms; H: −0.43 ms; I: 0 ms; J: 0.25 ms; K: 0.45 ms; L: 0.68 ms; M: 0.9 ms; N: 1.1 ms; O: 1. 3 ms; P: 1.9 ms. The drop shape images are obtained by processing high-speed video in IMAGEJ software [20]. The parameters of the experimental observations are the same as those given in Fig. 2.

pole if the gravity acts from north to south). Out of the 49 breakup events observed, 42 cases resulted in upward ejection, whereas the rest exhibit downward ejection. About 24–30% charge loss is observed in the breakup, similar to that reported in the literature [4,21–25]. The fact that a large number of frames captured in different stages of the charged droplet breakup process, observed through high-speed imaging of a single drop, makes it possible to compare the observations with continuous-time evolution models of the entire process. This constitutes a major distinguishing feature of this work.

The video images (see Fig. 3) raise four major questions: (i) How are the CM motion and the shape deformations related, and how do they affect the breakup pathway of the drop? (ii) Why does the droplet breakup predominantly occur in one direction (upward, at the north pole)? (iii) How is the critical charge required to induce the instability modified due to CM-surface oscillations coupling? (iv) What is the role of the external quadrupolar potential on the droplet destabilization? To answer these questions, it is necessary to analyze all the stages observed in the breakup process, including center-of-mass oscillations, dynamics of surface oscillations in the quadrupole trap and the physics of upward breakup and these are discussed in detail in the following sections.

V. DISCUSSION

A. Center-of-mass motion

The droplet in our experiments is levitated in a purely AC quadrupole potential [15], unlike the previous study [26] where the weight of the charged drop is balanced by an additional DC bias voltage. In the theoretical description of the problem, the weight of the droplet therefore appears in the z-directional (the direction of gravity) equation of motion, which is a modified Mathieu equation on account of the grav-

ity and the frictional drag, as

$$z''(\tau) + cz'(\tau) - a_z z(\tau)\cos(\tau) + \frac{g}{\omega^2} = 0. \tag{8}$$

Here, the trap potential given by Eq. (1) is used, where the center of the coordinate system coincides with the geometric center of the trap, and the droplet undergoes z-directional CM motion. Here, $a_z = 2Q\Lambda_0/(\frac{4\pi}{3}r_d^3\rho_d\omega^2)$, $c = 6\pi r_d \mu_a/(\frac{4\pi}{3}r_d^3\rho_d\omega)$, τ $(=\omega t)$ is the nondimensional time, $\omega = 2\pi f$, f is the frequency of the applied AC field, ρ_d is the density of the drop, μ_a is the viscosity of the air, and Q is the charge on the drop. It should be noted that z in Eq. (8) is kept dimensional so that it can be directly compared with the experimental observations. All the required parameters can be obtained from experiments, except the charge on the drop which can be determined indirectly by one of the two methods described below.

With respect to CM stability of the droplet, a droplet can get loosely levitated with lower CM stability ($a_z \sim 0.25$) with large CM oscillations. As the droplet evaporates with time, the mass of the droplet decreases, thereby increasing the value of stability parameter a_z. When a_z reaches a critical value ($a_{z,\text{critical}} \sim 0.445$, at $c \sim 0$), the CM oscillations become violent (known as spring oscillations [27]) and the droplet tries to escape the ED balance. Thus, to re-stabilize the droplet, the applied frequency is increased, which reduces the value of a_z. In most of the experiments (80% of all the experiments), the frequency is adjusted such that the droplet is levitated at a value just below its critical stability limit ($a_z \sim 0.4$–0.44). Thus an approximate value of the charge on the droplet can easily be obtained from the definition of a_z. The value of Q calculated from the definition of a_z using all other measured experimental parameters yields Q of the order of Rayleigh charge (Q_R), clearly indicating that the droplet is charged near the Rayleigh limit.

Alternately, when a bigger sized droplet is levitated at a lower value of a_z, due to its high initial charge, the droplet breaks before it undergoes spring oscillations. In this case, the charge on the droplet can be estimated by fitting the value of the charge in the modified Mathieu equation to match the experimentally obtained amplitude of the CM oscillations, as shown in Fig. 4(a). It is interesting to note that the value of charge fitted to match the amplitude of the CM oscillations in the experiments is nearly equal to the Rayleigh limit of charge within ±10%, which can be attributed to experimental error ($Q \sim Q_R$).

Thus, although the above methods can be used to determine the charge on the droplet, and suggest a near Rayleigh charge, the accuracy is limited, especially when attempting to explain subcritical instabilities. Hence, as will be discussed, recourse will be taken by BEM simulations to ascertain the same.

The above calculations are reported for a positively charged droplet. It is pertinent to mention here that for the discussion presented in this work we consider the droplet to be positively charged. It is easy to note that the discussion can be extended to a negatively charged droplet with appropriate reversal of the signs of the end caps and ring electrodes. A few experiments were indeed conducted to ensure that the phenomenon is independent of the sign of the charged droplet.
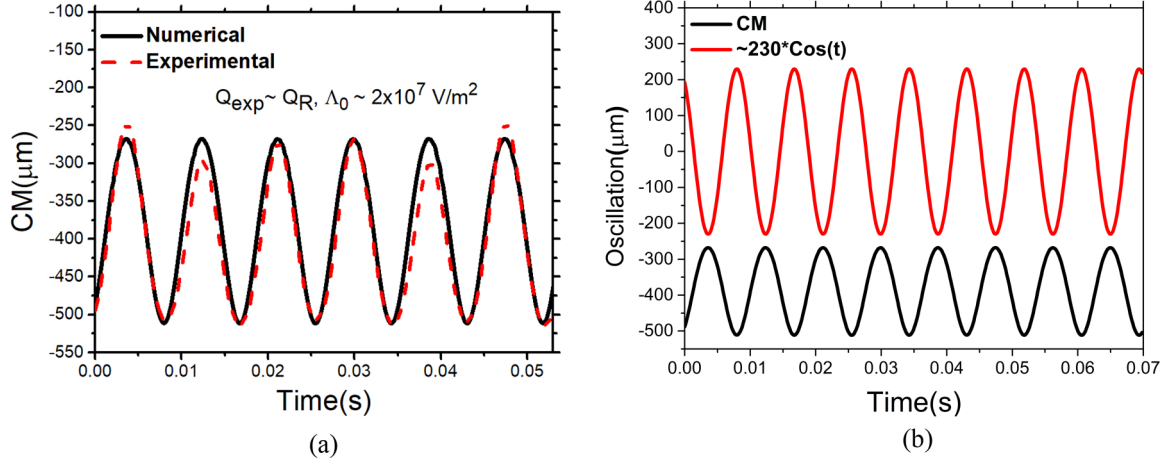
(a)

(b)

FIG. 4. (a) Comparison of CM motion obtained from numerical solution of Eq. (8) and experimental image processing. The values of parameters used for numerical solution are borrowed from experimental observation as indicated in the figure. (b) The variation of CM and applied AC field with time as obtained from the numerical solution. The parameters used are the same as those given in Fig. 2.

The CM oscillations can also be used to get the approximate z-directional shift (z_{shift}) of the drop from the center of the trap. From Fig. 4(a) the maximum value of z_{shift} estimated as ~500 μm. The droplet is found to oscillate below the center of the trap and remains bounded between the center of the trap and the south end cap [as shown Fig. 1(a)]. Note that the end cap is located at 10 000 μm in the experimental setup used in this work. The time-averaged equilibrium position of the droplet ($\langle z_{shift} \rangle = \bar{z}$) can also be obtained from the simple force balance in the z direction. The expression of $\bar{z}$ in terms of the trapping parameters can be found in the Supplemental Material (SM) [28].

The important observation here is that, when the droplet is stabilized at an off-centered position, it oscillates with the applied frequency (ω) around its equilibrium position [Fig. 4(a)], experiencing a local uniform electric field ($E = 2\Lambda_0 z_{shift}$) along with a nonzero quadrupolar electric field (Λ). The amplitude of these CM oscillations and E are proportional to z_{shift}. In contrast, when the droplet is stabilized exactly at the center of the trap by annulling the force of gravity with a DC field [4], it experiences negligible influence of the external quadrupolar fields and thereby exhibits small amplitude CM oscillations. This apparently minor difference has a significant effect on the nature of droplet surface destabilization.

The electrostatic force acting on a positively charged drop that exhibits oscillations in its CM motion sensitively depends upon the relative position of the charged drop within the trap, with respect to the oscillatory potential of the south end cap. The numerical solution of Eq. (8) is plotted as a function of time along with the applied AC cycle, as shown in Fig. 4(b). It can be observed that, in the positive AC cycle, the position of the drop is lowest, i.e., near the south end-cap electrode

[maximum negative displacement; also see Fig. 2(i)]. This indicates that there is a phase shift of π between the CM motion and the applied field. It will be seen later that the π phase shift and the large amplitude CM oscillations of the droplet have an important implication for the asymmetric breakup of the droplet. The exact phase lag between the applied AC field and the CM motion could not be measured in the experiments. The comparison is made possible by synchronizing the peak position of the deformation [Fig. 2(ii)] to the negative peak of the AC cycle [Fig. 2(i)] at early times.

B. Dynamics of surface oscillation

The equations governing the dynamics of surface oscillation of the levitated charged droplet [29] in a quadrupole trap are obtained from a leading order asymptotic theory with respect to small amplitude of oscillations. The surface of the droplet is described as $r_s(t, \theta)$ in terms of Legendre modes with α_l as the perturbation coefficient. The coefficient α_1 represents the CM motion, α_2 and α_4 indicate symmetric dipolar and quadrupolar shape deformations, respectively, and the coefficient α_3 is a measure of asymmetric shape deformation. The experimental observations of the oscillatory shape deformations can be described by a potential theory with viscous corrections [29], and these viscous corrections (which suppress high-frequency capillary oscillations) are found to be critical to explain the experimental observations. To linear order in shape coefficients and small displacements of CM, we assume that the droplet experiences a quadrupolar field given by Eq. (1) and that the droplet is levitated at z_{shift}, where it experiences a uniform electric field $E = 2\Lambda_0 z_{shift}$. This allows us to write the governing equations for shape coefficients in the limit of small deformations as

$$\alpha_2''(t) + \frac{6}{3\beta + 2}\left(2(\lambda + 4)\text{Oh}\,\alpha_2'(t) + 4\alpha_2(t) - 3\text{Ca}_E\,\zeta^2 + 10X\sqrt{\text{Ca}_\Lambda}\,\zeta - \frac{25\text{Ca}_\Lambda\,\zeta^2}{7}\right) = 0, \tag{9}$$

$$\alpha_3''(t) + \frac{1}{4\beta + 3}\left(24(2\lambda + 5)\text{Oh}\,\alpha_3'(t) + 120\alpha_3(t) - 108\sqrt{\text{Ca}_E}\sqrt{\text{Ca}_\Lambda}\,\zeta^2\right) = 0, \tag{10}$$

$$\alpha_4''(t) + \frac{1}{5\beta + 4}(840(\lambda + 2)\text{Oh}\,\alpha_4'(t) + 2520\alpha_4(t) - 900\text{Ca}_\Lambda\,\zeta^2) = 0, \tag{11}$$
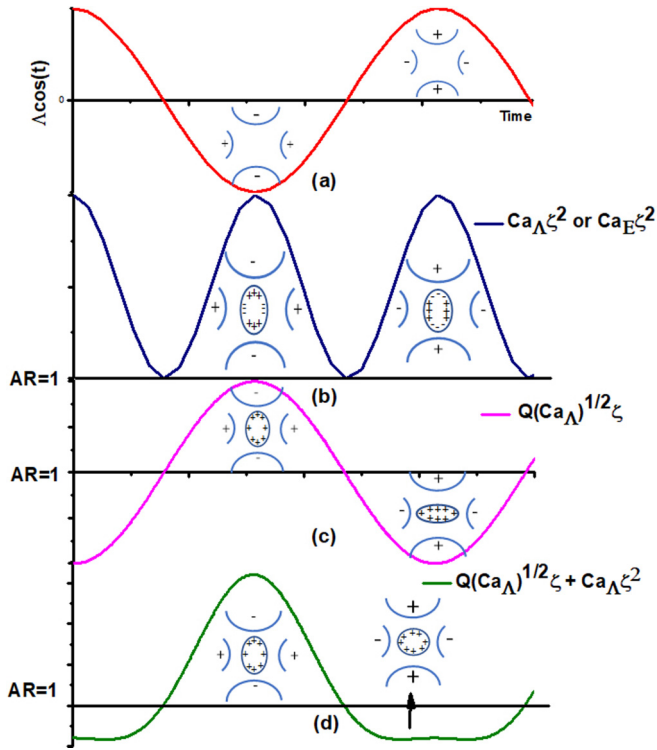
FIG. 5. A schematic representation of the effect of various electrical parameters on shape oscillation characteristics of the droplet: (a) applied AC signal, (b) oscillations of a neutral drop in the presence of quadrupole and/or uniform field, (c) oscillation of highly charged drop levitated exactly at the center of the quadrupole trap, (d) oscillation of a moderately charged drop levitated at a position away from the center of the trap in the presence of a quadrupole potential.

where $Oh = \mu_d/\sqrt{\gamma r_d \rho_d}$ is the Ohnesorge number, $\beta = \rho_a/\rho_d$ is the density ratio between the droplet and the surrounding medium, $X = Q/Q_R$ is the fissility, $Ca_\Lambda = (r_d^3 \epsilon_e/\gamma)\Lambda_0^2$, and $Ca_E = (r_d \epsilon_e/\gamma)E^2$, where Ca_Λ and Ca_E are the forces due to quadrupolar potential and uniform fields respectively. The effect of several electrical force terms such as $\sqrt{Ca_E}\sqrt{Ca_\Lambda}$ (asymmetric force on an uncharged drop due to uniform field and field due to quadrupole potential coupling) and $Q\sqrt{Ca_\Lambda}$ (force on a charged drop due to quadrupole potential) on the characteristics of surface dynamics [Fig. 2(ii)] can be understood by solving Eqs. (9), (10), and (11) simultaneously. A schematic representation of effect of various parameters and forces on the characteristics of a charged droplet oscillations is shown in Fig. 5. Fig. 5(a) is a variation of the applied potential with respect to time. If the value of $\Lambda(t)$ is positive the end-cap potential is positive and vice versa.

The shape oscillations of an off-centered *uncharged drop* in a quadrupole trap are caused by Ca_Λ and Ca_E. Ca_Λ induces both dipolar and quadrupolar shape oscillations with a frequency of 2ω while, Ca_E (due to off-center position) excites dipolar oscillations with a frequency 2ω. These forces induce the polarization of the free charges in a neutral drop, and the droplet oscillates with the frequency of 2ω [Fig. 5(b)]. On the other hand, the quadrupolar field acting on the to-

tal unperturbed charge (Q) of the undeformed drop leads to symmetric shape deformations with frequency ω due to the $\sqrt{Ca_\Lambda}Q$ term as shown in Fig. 5(c). The experiments (Fig. 2) indicate that the shape oscillations occur at frequency ω with weak oblate deformations, thereby suggesting a complex interplay between the shape deforming terms $\sqrt{Ca_\Lambda}Q$, Ca_Λ, and Ca_E, where the first term contributes a ω response, the latter two terms contribute to the superimposed 2ω response. This has been elucidated in Fig. 5(d).

The shape deformations can also be understood in terms of the electrostatic attraction or repulsion between the charge on the droplet and the polarity of the electrodes. When the applied potential is positive (and maximum), the positively charged droplet experiences maximum electrostatic repulsion from the end cap electrodes and deforms the droplet into an oblate shape (AR < 1). Similarly, in the negative AC cycle, the droplet experiences electrostatic attraction from the end cap electrodes and deforms into a prolate spheroid (AR > 1) [Fig. 5(c)]. Using this reasoning, the peak negative potential of the AC cycle is made to coincide with the peak prolate amplitude of the shape deformation observed in the experiments, so as to match the temporal evolution of deformation with the applied field, and has been reported elsewhere [29].

C. Droplet breakup

In the course of executing both the CM and shape oscillations, the evaporation of the droplet can cause the droplet charge to approach its Rayleigh limit, leading to the onset of Rayleigh instability, which eventually leads to an asymmetric breakup via the formation of a jet (movie, SM [28]). We consider a positively charged droplet for convenience of arguments, and it should be noted that the physics is unaltered for a negatively charged droplet. Thus, considering a positively charged droplet levitated using an AC quadrupole field, the relative potential (either positive or negative) of the end cap and the corresponding deformation are critical to asymmetric breakup. While the quadrupolar field Λ_0 corresponding to that acting at the center of the drop can only induce symmetric deformation in the drop and thereby a possible symmetric breakup [as shown in Figs. 6(a) and 6(b)], any asymmetric breakup should occur due to the differential, locally uniform field E acting on the surface of an off-centered droplet [as shown in Figs. 6(c) and 6(d)]. A positively charged droplet near a positive south end cap should deform into an oblate spheroid due to the electrostatic repulsion at the poles between the like-charged drop and the end cap as well as due to the electrostatic attraction between the oppositely charged drop and the ring electrode at the equator [Fig. 6(d)]. On the other hand, if a positively charged drop is near the negative south end cap [Fig. 6(c)] it should break in the downward direction due to higher electrostatic attraction from the south end cap and repulsion from the ring electrode [as shown in Fig. 6(c)]. It is also possible that a positively charged droplet near a positively charged end cap could attain an oblate shape [Fig. 6(d)].

The experiments show that the breakup is predominantly asymmetric, with a majority of jet ejection events occurring upwards [at the north pole, against gravity, as shown in Figs. 3 and 6(e)] (also see SM [28]). With the above possible scenarios (Fig. 6), the predominance of the upward breakup
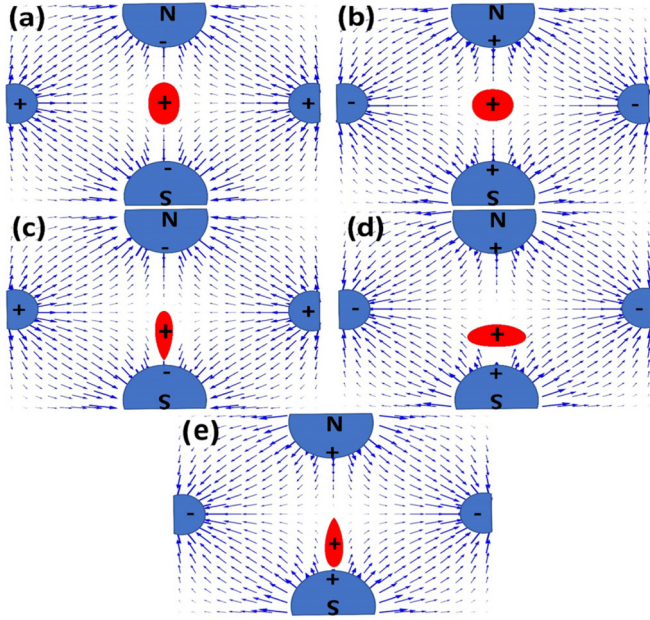
FIG. 6. Schematic representation of polarity of electrodes, droplet position, and corresponding deformation leading to breakup. Panels (a) and (b) show the drop at the center of the trap and symmetric deformation, whereas panels (c) and (d) show the drop at an off-centered position with endcap polarity dependent deformation and breakup.

is somewhat intriguing, and its understanding requires careful theoretical analysis of the problem. Therefore, to further understand the underlying mechanism and the stresses responsible for the asymmetric breakup, we performed numerical simulations using the axisymmetric boundary element method (BEM). The asymptotic analysis in small Λ [Eqs. (9)–(11)], indicates that the oscillations associated with the natural frequency are quickly damped such that at long times, the oscillation frequency is the same as the applied frequency [29]. Moreover, at the onset of jet ejection, the rate of change of AR values predicted by the simulations (presented in our previous work [17]) in the viscous limit is in good agreement with those observed in the previously reported experiments [5]. Therefore, to understand the mechanism of droplet deformation and breakup, BEM calculations are carried out in the viscous flow limit. Additionally, experiments indicate that the breakup of the droplet is very fast and occurs at around $1/10$ of the timescale associated with the time period of the AC signal. In view of this, the simulations are carried out by considering either positive or negative DC quadrupole potential with the intensity of the applied electric field Λ_0. All the parameters are borrowed from direct observations of the experiments, and the value of z_{shift} is taken as the maximum displacement observed from Fig. 4(a), i.e., $\sim 500 \mu$m.

A systematic set of simulations (see the Appendix A) addressing different scenarios corresponding to Figs. 6(c)–6(e) are then performed to understand the underlying mechanism. The numerical analysis depicting the effect of various initial perturbations, charge on the drop, polarity of the endcap electrodes and position of the droplet in the trap on

the breakup characteristics is summarized in the Appendix (Table I).

We first conduct calculations with an initially spherical droplet. The simulations indicate that, at Rayleigh charge (i.e., 8π) with a downward z_{shift} and an unperturbed initial spherical shape, the drop breaks in the downward direction for negative end-cap potential. The observation is explained by the fact that in the vicinity of a negative end cap the positive charges accumulate at the south pole of the drop due to electrostatic attraction between charges on the drop and the end-cap electrode. Due to the accumulation of charges, the droplet develops high curvature at the south pole, which leads to a downward breakup for experimentally relevant parameters (Appendix Table I case 2).

Secondly, an analysis of the CM motion on the levitated charged droplets indicates that most often, the droplet breakup occurs when the droplet is near the south end-cap electrode (see SM [28]). Experiments [Fig. 2(i)] also show that the positively charged droplet is in the vicinity of the south end cap when the latter is at positive peak potential. This is attributed to the phase lag of π between the applied potential and the CM motion. Thus one can conclude that the case (2) in Table I [also indicated in Fig. 6(c)] is rarely encountered. Therefore, we consider the case of an initially spherical droplet near an end cap with positive potential, with the drop exhibiting a downward z_{shift}. The positively charged drop now experiences an electrostatic repulsion from the end-cap electrode as well as attraction from the ring electrode. Thus, in this configuration, the droplet renders a stable oblate shape and cannot undergo breakup for typical experimental parameters [Appendix Table I case 3, Fig. 6(d)].

These results contradict the experimental observation where the droplet breaks in the upward direction in the positive cycle of the applied field (which corresponds to positive end-cap potential). The apparent inconsistency can be resolved by observing that in Figs. 2(ii) and 3, at point G, which is the droplet state just before the breakup, the droplet exhibits a highly deformed prolate spheroidal shape and does not undergo prolate-to-oblate oscillations thereafter. As at this point, the droplet has built a near critical charge to admit Rayleigh instability that leads to a breakup. We therefore consider this point to be the onset of the Rayleigh instability, and investigate several scenarios.

In the first case, we consider the experimentally observed drop shape corresponding to image G in Fig. 3 as an initial shape in the numerical calculations. The outline of the drop shape in image G is obtained using the IMAGEJ software and is fitted using the nonlinear least-square method to a Legendre series (using *Mathematica* software, version 10) to obtain the coefficients of the different Legendre modes. The details of the shape fitting analysis can be found in SM [28]. The coefficient of the second Legendre (P_2) mode is thus obtained as 10.56μm and that of the third Legendre (P_3) mode as $+2.08 \mu$m, and the radius (r_d) of the undeformed drop is 108μm. The shape fitting indicates that the symmetric P_2 mode is most prominent. Incidentally, P_2 is the most unstable mode as predicted by the linear and nonlinear analysis of Rayleigh breakup of a charged drop [10,30]. A significant value of the asymmetric P_3 mode is also observed (a

positive value of P_3 mode means a higher curvature at the north pole and vice versa). The simulations are initialized with a shape corresponding to image G (Fig. 3) where the initial shape of the droplet considered in the simulations is perturbed with the coefficients of P_2 and P_3 modes, obtained from the experiments. For numerical simulations the parameters are nondimensionalized with r_d and are given as $Ca_\Lambda = 0.00058$, $z_{shift} = 4.63$, $\alpha_2 = 0.1$, $\alpha_3 = 0.02$.

The BEM calculations are carried out by providing an initial surface charge Q to this perturbed shape (the perturbation is obtained form the experimental drop shape) drop at a value which is in the sub-Rayleigh charge limit and progressively increasing it till the critical (i.e., minimum) value of the charge at which the droplet undergoes breakup (cases 4-7 in Table I).

If the charge is less than this critical value, the droplet relaxes back to the spherical shape (Appendix Table I case 4). However, when the charge is around the critical value (cases 5-7 in Table I), the initial shape perturbations grow, and the droplet evolves to form sharp conical ends, finally admitting a numerical singularity [17]. It is found that the droplet breaks at 98.7% (i.e., 7.9π) of the Rayleigh charge for the given parameters. The breakup at subcritical charge clearly demonstrates that subcritical Rayleigh instability can be induced by finite-amplitude perturbations. Since the external electric field is small, it acts as a trigger for inducing surface perturbations and has an insignificant role in causing break up. This is in line with the prediction of the theory that the breakup of a droplet in the quadrupole electric field is a transcritical bifurcation [12].

To understand the mechanism more clearly, a closer look at the role of initial perturbation suggests that, for an initial shape with dominant P_2 perturbation and a positive P_3 perturbation, the breakup is always observed in the upward (at the north pole) direction when the end cap is positive, in conformity with experiments (Appendix Table I case 5). Under these conditions, there can be two mechanisms responsible for asymmetry in the droplet shape at the onset of the breakup.

First, a significant positive α_3 perturbation (for the P_3 mode) in the initial droplet shape can assist upward and asymmetric breakup (Appendix Table I case 5).

Second, although initially $\alpha_3 = 0$, an α_3 perturbation can develop due to the nonlinear interaction between the dipolar charge distribution on the drop and the positive (when the south end cap is positive) uniform electric field (E) experienced by the prolate spheroidal droplet, or the $\sqrt{Ca_E}\sqrt{Ca_\Lambda}$ term in the evolution equation for α_3 in Eq. (10) (Appendix Table I case 8).

When simulations are carried out even in absence of an initial P_3 perturbation, case 8, the subsequent manifestation of the P_3 mode leads to an upward (north pole) asymmetric deformation and subsequent breakup. Since the magnitude of α_3 depends on the strength of the coupling between α_2 and E (which takes a certain amount of time to become significant), the asymmetry manifests at a later stage in the dynamics of the drop breakup. This explains the late onset of asymmetric breakup seen in Fig. 7.

The above reasoning may be quantified by examining the time evolution of normal stresses acting on the surface of the drop (see Fig. 8) using the BEM method. Initially, when the drop is perturbed with experimentally obtained values of
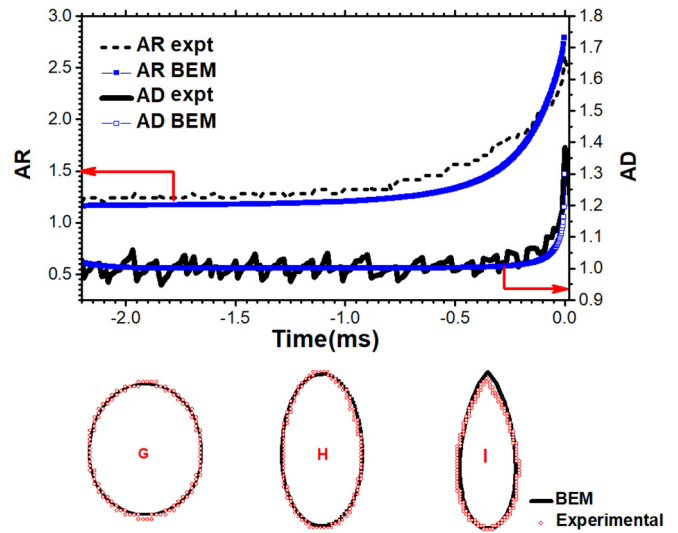

FIG. 7. Comparison of experimental observations with BEM simulations for temporal evolution of AR and AD along with the drop shapes at three different times near the breakup (shown in the bottom panel).

shape deformation coefficients, the normal electric stresses acting on the drop surface are only marginally higher at the north pole. As may be seen in Fig. 8, the stress distribution remains nearly symmetric for a considerable time (between $t = -2.2$ and -0.15 ms). The nearly symmetric stress distribution also corresponds to nearly symmetric dipolar (P_2) charge distribution. Beyond this point ($t = -0.15$), the interaction between P_1 and P_2 escalates, creating an asymmetric (P_3) charge distribution and thereby asymmetric Maxwell stress distribution, which through a feedback mechanism manifests as an asymmetric upward breakup. The asymmetry is thus a result of the finite-amplitude perturbation of the symmetric mode, and therefore the AD manifests later (as compared to AR) in the instability. The mechanism prevails even when the initial perturbation does not have the P_3 mode ($\alpha_3 = 0$), thereby explaining why the upward breakup is more prevalent in experiments.
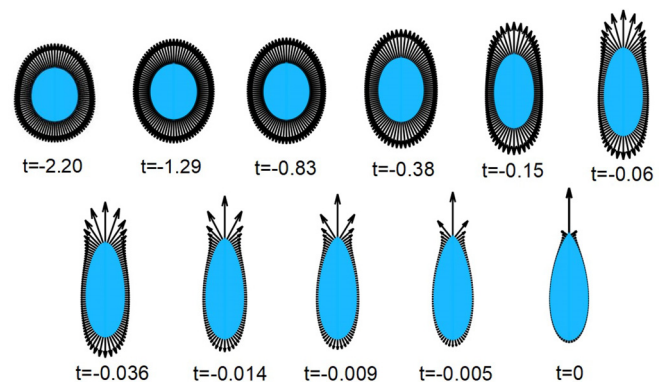

FIG. 8. The stress distribution on the surface of the drop obtained from BEM simulation. The numbers indicated below the drop shapes are times in milliseconds.

The droplet shape evolution predicted by BEM simulations is compared with the experimental observations, as indicated by AR and AD. A remarkable agreement is observed between the experiments and the simulations (Fig. 7), including the important observation of a late onset of asymmetry. Moreover, the shapes of the drop from the critical point (G) to the breakup point (I) are accurately predicted by the BEM simulations, as shown in Fig. 7. The drop shape corresponding to the image I is compared without considering the jet part observed in the experiments since the BEM calculations for perfect conductor drop cannot capture the jet formation. To predict the jet and progeny formation in the breakup of charged drops, it is necessary to consider the finite charge dynamics on the drop surface [31]. Since in this study BEM simulations are carried out for the understanding of the underlying mechanism of the experimentally observed asymmetric breakup of highly conducting charged drops, the finite surface charge dynamics is neglected.

In certain cases (in about 10% of the cases) where α_3 is negative, a downward breakup has been observed. This can be explained as follows: although a phase shift of π is observed between the applied AC field and the CM oscillations, in few experiments, we observe that the south end cap is at negative potential when the droplet is at the bottom of its CM motion and attains a critical shape. Moreover, the shape at this stage also indicates a negative α_3 (for details see SM [28]). Since this situation is rare, fewer droplets are found to break in the downward direction.

VI. CONCLUSIONS

While the work of Duft *et al.* [4] has shown pioneering evidence for a symmetrical pathway for Rayleigh breakup, the present study shows that this is not universal, and perhaps is an exception in realistic situations. Specifically, by considering the effect of gravity and external electric fields and from the insight obtained by numerical calculations, an asymmetric breakup might turn out to be the rule in real-life practical situations, such as the one that is commonly encountered in nanodrop generators using electrosprays. This is amply demonstrated through continuous high-speed imaging of levitated drops in a quadrupole trap combined with BEM simulations. The external electric fields act as initiators of finite-amplitude shape deformations, which assist in driving the droplets towards subcritical Rayleigh breakup even when the charges carried by them are less than the Rayleigh critical charge. BEM calculations accurately predict these values to be about 98–99% of the Rayleigh limit in conformity with experimental observations. It must be pointed out that detailed bifurcation diagrams exist for Rayleigh instability, and these clearly include transcritical bifurcations at $Q = Q_R$ [10,12] as well as imperfect transcritical bifurcations in the presence of walls [32]. The prolate and oblate deformations correspond to sub- and supercritical bifurcations, respectively. The present observations are in conformity with a previous study that showed that the applied quadrupole potential could further reduce the critical Rayleigh charge due to an interaction between the applied field and the Rayleigh instability [12]. The external fields also induce asymmetric jet ejection, and the study shows that there is a strong shape instability coupling in the dynamics of charged drops.

The study has a far-reaching bearing on technologies exploiting the Rayleigh breakup process for nanoparticle generation using electrosprays, or ion mass spectrometry. The occurrence of subcritical break up will influence the history, and asymmetric break up will affect the evolution of the spatial distribution of droplet sizes. Moreover, judicious choice of the polarity of confining electrodes can lead to greater effectiveness in the breakup of droplets. All these practical implications of the findings presented here deserve careful consideration in future studies.

The sizes of the ejected droplets could not be measured very accurately due to the limitation of the resolution of the microscopy used in our experiments. However, looking at at the hazy droplet images provides an approximate estimate of the daughter droplet size as $\sim 5 \pm 4 \ \mu$m. The daughter droplets move away from the observational field of view within 10–20 μs after their ejection due to electrostatic repulsion from the mother droplet. As a result, it is not possible to make direct observations on the fate of the daughter droplets. However, based on the observations and analysis of the breakup pathway of the mother droplet, it is reasonable to expect that the ejected daughter droplets would undergo further breakup, giving rise to yet smaller satellite droplets, and so on. This, however, needs further careful investigation.

APPENDIX: RESULTS OF EXTENDED BEM SIMULATIONS

For different values of forcing parameter, i.e., intensity of quadrupole electric field, Ca_Λ, the mode of droplet breakup is significantly different. For the numerical analysis of drop breakup, the strength of forcing parameter is borrowed from the actual experimental parameters, i.e., $Ca_\Lambda = 0.00058$ and is used in BEM simulations. In simulations if the forcing term (Ca_Λ) is arbitrarily increased by 10 times, it is observed that in the presence of high positive Λ_0 the positively charged drop deforms into oblate spheroid and remains stable even for charge higher than the Rayleigh limit ($Q > 8\pi$). This is basically due to high electrostatic repulsion exerted by the south end cap at positive potential on the positively charged drop. A value of Ca_Λ much lower than 0.00058 does not affect the drop deformation significantly and the drop breaks symmetrically.

Thus, the value of Ca_Λ is kept constant at 0.00058 and all the other situations that can arise during the experiments with respect to direction of applied electric field, position of the drop in the trap, and initial perturbations are analyzed using BEM simulations. The results are summarized in Table I. From the table it can be observed that the downward breakup is a special case that occurs only when Λ is negative.

TABLE I. Summary of initial conditions and breakup behavior of a charged drop levitated in the quadrupole trap. Position of the drop in the trap is abbreviated as COT (center of trap) or NSEC (near south end cap) and SN represents simulation number.

SN	Initial shape perturbations	Charge (Q)	Position	Sign of Λ	Result
1	$\alpha_2 = \alpha_3 = 0$	8π	COT	Positive/Negative	Symmetric breakup
2	$\alpha_2 = \alpha_3 = 0$	8π	NSEC	Negative	Downward breakup
3	$\alpha_2 = \alpha_3 = 0$	8π	NSEC	Positive	Stable oblate
4	$\alpha_2 = 0.1, \alpha_3 = 0.02$	$<7.9\pi$	NSEC	Positive	Stable sphere
5	$\alpha_2 = 0.1, \alpha_3 = 0.02$	7.9π	NSEC	Positive	Upward breakup
6	$\alpha_2 = 0.1, \alpha_3 = 0.02$	7.9π	NSEC	Negative	Downward breakup
7	$\alpha_2 = 0.1, \alpha_3 = -0.02$	7.9π	NSEC	Positive	Symmetric breakup
8	$\alpha_2 = 0.1, \alpha_3 = 0.0$	7.9π	NSEC	Positive	Upward breakup
9	$\alpha_2 = 0.1, \alpha_3 = 0.0$	7.9π	NSEC	Negative	Downward breakup

As argued in the article, this, however, is a less probable condition. Thus simulations also indicate that when Λ is positive, which is the more probable case, the breakup is upward as also seen in most experimental observations. Interestingly, even in the absence of initial P_3 perturbation in the drop shape, the droplet breakup occurs with an upward asymmetry when the charge is sub-Rayleigh, demonstrating subcritical breakup of charged droplets.

[1] L. Rayleigh, London Edinburgh Dublin Philos. Mag. J. Sci. **14**, 184 (1882).

[2] B. J. Mason, Proc. R. Soc. London, Ser. A: Math. Phys. Sci. **327**, 433 (1972).

[3] J. B. Fenn, M. Mann, C. K. Meng, S. F. Wong, and C. M. Whitehouse, Science **246**, 64 (1989).

[4] D. Duft, T. Achtzehn, R. Müller, B. A. Huber, and T. Leisner, Nature (London) **421**, 128 (2003).

[5] E. Giglio, B. Gervais, J. Rangama, B. Manil, B. A. Huber, D. Duft, R. Müller, T. Leisner, and C. Guet, Phys. Rev. E **77**, 036319 (2008).

[6] P. Adornato and R. Brown, Proc. R. Soc. London, Ser. A: Math. Phys. Sci. **389**, 101 (1983).

[7] N. Pelekasis, J. Tsamopoulos, and G. Manolis, Phys. Fluids A **2**, 1328 (1990).

[8] R. Natarajan and R. Brown, Proc. R. Soc. London, Ser. A: Math. Phys. Sci. **410**, 209 (1987).

[9] J. Tsamopoulos, T. Akylas, and R. Brown, Proc. R. Soc. London, Ser. A: Math. Phys. Sci. **401**, 67 (1985).

[10] O. Basaran and L. E. Scriven, Phys. Fluids A **1**, 795 (1989).

[11] S. Betelú, M. Fontelos, U. Kindelán, and O. Vantzos, Phys. Fluids **18**, 051706 (2006).

[12] S. Das, Y. S. Mayya, and R. Thaokar, Europhys. Lett. **111**, 24006 (2015).

[13] N. Pelekasis and J. Tsamopoulos, Eng. Anal. Boundary Elem. **15**, 339 (1995).

[14] J. C. Burton and P. Taborek, Phys. Rev. Lett. **106**, 144501 (2011).

[15] M. Singh, Y. S. Mayya, J. Gaware, and R. M. Thaokar, J. Appl. Phys. **121**, 054503 (2017).

[16] S. D. Deshmukh and R. M. Thaokar, Phys. Fluids **24**, 032105 (2012).

[17] N. Gawande, Y. S. Mayya, and R. Thaokar, Phys. Rev. Fluids **2**, 113603 (2017).

[18] J. Sherwood, J. Fluid Mech. **188**, 133 (1988).

[19] C. Pozrikidis, *Boundary Integral and Singularity Methods for Linearized Viscous Flow* (Cambridge University Press, Cambridge, 1992).

[20] ImageJ software, https://imagej.nih.gov/ij.

[21] J. W. Schweizer and D. Hanson, J. Colloid Interface Sci. **35**, 417 (1971).

[22] M. Abbas and J. Latham, J. Fluid Mech. **30**, 663 (1967).

[23] M. Roulleau and M. Desbois, J. Atmos. Sci. **29**, 565 (1972).

[24] A. Doyle, D. R. Moffett, and B. Vonnegut, J. Colloid Sci. **19**, 136 (1964).

[25] H. C. Hunter and A. K. Ray, Phys. Chem. Chem. Phys. **11**, 6156 (2009).

[26] D. Duft, H. Lebius, B. A. Huber, C. Guet, and T. Leisner, Phys. Rev. Lett. **89**, 084503 (2002).

[27] S. Ataman and D. Hanson, Ind. Eng. Chem. Fundam. **8**, 833 (1969).

[28] See Supplemental Material at http://link.aps.org/supplemental/10.1103/PhysRevE.103.053111 for derivation of the theoretical estimation of z_{shift}, details of shape fitting analysis, CM oscillations, a few more experimental observations of upward and downward breakup, time evolution of various shape modes obtained from extended numerical calculations, and high-speed video evidence of a subcritical asymmetric Rayleigh breakup event.

[29] M. Singh, N. Gawande, Y. S. Mayya, and R. Thaokar, Phys. Fluids **30**, 122105 (2018).

[30] R. Thaokar and S. Deshmukh, Phys. Fluids **22**, 034107 (2010).

[31] N. Gawande, Y. S. Mayya, and R. Thaokar, J. Fluid Mech. **884**, A31 (2020).

[32] S. Mhatre, S. Deshmukh, and R. Thaokar, Eur. Phys. J. E **35**, 1 (2012).